

Massive Quiescent Cores in Orion. I. Temperature Structure

D. Li^{1,2}, P. F. Goldsmith², and K. Menten³

ABSTRACT

We have mapped four massive cores in Orion using the NH_3 (J,K) = (1,1) and (J,K) = (2,2) inversion transitions, as part of our effort to study the pre-protostellar phase of massive star formation. These cores were selected to be quiescent, i.e. they contain no apparent IR sources and are not associated with any molecular outflows. These cores are one order of magnitude more massive than dark cloud cores and have about twice the line width. This paper focuses on their temperature structure. We find a statistically significant correlation between the gas kinetic temperature and the gas column density. The general trend is for the gas to be colder where the column density is higher, which we interpret to mean that the interiors of these cores are colder than the regions surrounding them. This is in contrast with dark cloud cores, which exhibit relatively flat temperature profiles. The temperature gradient within the massive quiescent Orion cores is consistent with an external radiation source heating the dust, and dust-gas collisions providing relatively close coupling between dust and gas temperatures. Thus, we suggest that the initial stage of massive pre-protostellar cloud cores is relatively quiescent condensations which are cooler than their surroundings.

Subject headings: ISM:clouds – individual (Orion) – radio line:ISM

1. INTRODUCTION

There appears to be a clear observational dichotomy between low mass star formation (LMSF) and high mass star formation (HMSF). HMSF only occurs in giant molecular clouds (GMC), while LMSF occurs in a variety of environments, including isolated Bok globules (Yun & Clemens 1990). No young star more massive than $2 M_\odot$ has been found in Taurus,

¹Center for Astrophysics, 60 Garden Street, Cambridge MA 02138, dli@cfa.harvard.edu

²National Astronomy and Ionosphere Center, Department of Astronomy, Cornell University, Ithaca NY 14853

³Max-Planck-Institut für Radioastronomie, Auf dem Hügel 69, 53121 Bonn, Germany

while both O stars and low mass stars are abundant in Orion (e.g. Muench et al. 2002). The comparison between the two types of regions shows that regions with HMSF have a higher efficiency in converting interstellar medium (ISM) mass into stellar mass. A particularly spectacular star forming theater is the Orion Nebula, where more than 2×10^3 young stars are contained in a radius of about 0.2 pc centered on the Trapezium O star cluster (Jones & Walker 1988; Hillenbrand & Hartmann 1998).

Star formation is correlated with dense molecular gas (e.g. Ungerechts & Thaddeus 1987). Particular attention has thus been focused upon dense structures, so called “cores”, within molecular cloud complexes as they may be sites of future star formation. Here, the cores refer to structures usually prominent in high density tracers, e.g. CS and NH₃, with mass between that of a single star and of a stellar cluster (Walmsley 1995). The cores can be divided into cores in LMSF regions such as Taurus (e.g. Onishi et al. 1998), and cores in HMSF giant molecular cloud (GMC) regions such as Orion (Tatematsu et al. 1993). The ensemble of cold cores in Orion has twice the mean size (0.3pc), twice the line width, and almost an order of magnitude higher mean mass ($80 M_{\odot}$) than do the cores in LMSF regions (e.g. Benson & Myers 1989; Clemens & Barvainis 1988).

Can the difference in the parameters of molecular cores help explain the dichotomy in star formation? Theoretically, there is a promising suggestion regarding the initial energy balance between gravity and turbulent pressure support. For LMSF, the picture is relatively clear. A core starts in equilibrium, supported by magnetohydrodynamic (MHD) turbulence (Myers & Goodman 1988). The magnetic field slowly decouples from the cloud as a result of ambipolar diffusion (Shu, Adams & Lizano 1987; Basu & Mouschovias 1995). As the magnetic support weakens, collapse starts from the center (highest density) and propagates from the inside to the outside of the cloud (Shu 1977; Larson 1969; Penston 1969). Since the ‘inside out’ collapse propagates roughly at the sound speed, it is considered a ‘slow’ process, having a time scale on the order of 10^6 to 10^7 yr. For HMSF, the process needs to be faster, in order to be consistent with the observed rate of star formation in a region like Orion. The theoretical hypothesis is that the core starts in a *super-critical* state, in which gravity overwhelms internal support. Then, the cloud collapses quickly on a free fall time scale and no ambipolar diffusion is needed. It is worth noting that super-critical state may also be applicable to low mass cores. If a core is embedded in a cloud complex, the ambient pressure can be larger than a critical value above which no magnetohydrostatic equilibrium exists. For such super-critical cores, the linewidth is supersonic, the star formation time scale is a couple of free-fall times, and no ambipolar diffusion is needed (Nakano 1998). This alternative picture (supercritical cores, no ambipolar diffusion) of LMSF is more consistent with the empirical evidence concerning Orion cores than with those of Taurus cores. In Orion, LMSF is very common, although HMSF (through the effects of the massive stars

which result) dominates the morphology and conditions of the region.

Modeling the actual process of HMSF is a very demanding undertaking, due in part to the difficulties in dealing with non-equilibrium problems and in part to the lack of observational constraints. There are at least four obstacles to unraveling the complex process of high mass star formation. Firstly, it is fast. A relevant time scale is the stellar Kelvin–Helmholtz (KH) time scale,

$$t_{KH} = \alpha \frac{GM^2}{RL} , \quad (1)$$

where α is a factor of the order of unity depending on the density profile of the object, and M , L , and R are the stellar mass, luminosity, and radius, respectively. From both empirical evidence and theoretical considerations (Clayton 1983), there exist scaling laws of the form of $L \propto M^{3.5}$ and $R \propto M$, which simplify Eq. (1) as

$$t_{KH} \approx 19 \text{ Myr} \left(\frac{M}{M_{\odot}} \right)^{-2.5} . \quad (2)$$

Increasing the stellar mass from 1 M_{\odot} to 10 M_{\odot} reduces t_{KH} by a factor of 300. For stars more massive than 10 M_{\odot} , the KH time scales are less than 0.1 Myr. There is probably no pre-main-sequence phase for massive star formation. Secondly, HMSF is dynamic. Once hydrogen burning starts, the environment of the newly-formed star will be severely altered, thus precluding the study of its immediate precursor state. Thirdly, the molecular condensations possibly leading to HMSF are found in cloud complexes and are hard to properly identify. Finally, there are no HMSF regions as close as Taurus, the prototypical region for studying LMSF star formation.

From an observer’s point of view, we want to tackle the problem from its very beginning, the pre-protostellar phase. This study starts with the very basic objective of identifying massive cores in a HMSF region. Fifteen quiescent cores have been chosen from the CS survey of Orion by Tatematsu et al. (1993) based on the following criteria: 1) We are restricted to a nearby GMC and relatively large cores in order to resolve structures with the available beam size of about 50". Fortunately, there is an adequate selection of cores in Orion having diameters larger than 0.4 pc or 3'. 2) We avoid cores too close to Orion-KL where the energy output of young, massive stars has dictated the filamentary morphology of the surrounding material (Wiseman & Ho 1998). 3) There is some information on the cores in our sample suggesting they are relatively isolated and cool (no IR/YSO association), but no complete data sets or models have been obtained.

These cores have been mapped in multiple transitions of $C^{18}O$ and CS, the J=1–0 transitions of N_2H^+ , the (1,1) and (2,2) inversion transitions of NH_3 , and in the 350 μm dust continuum. The goal of is to retrieve most of the relevant physical parameters of these cores,

including size, mass, temperature, and density structure. The sources and their derived parameters are listed in Table 1. Additional data on these cores including their mass and density, is obtained from C¹⁸O and CS observations conducted at the Five College Radio Astronomy Observatory (FCRAO). These observations will be presented in detail in a later paper. Some information from FCRAO observations is included here to aid the analysis of the thermal structure presented in Sections 5 and 6. This paper will focus on the temperature structure of these cores obtained from NH₃ observations, while other aspects will be considered in subsequent work.

2. Kinetic Temperature and NH₃

The kinetic temperature is a crucial parameter for defining excitation conditions from multi-transition spectral line observations. In order to determine the column density accurately from tracers such as the C¹⁸O J=1–0 transition, a good knowledge of the gas temperature is also required. Together with volume density, the kinetic temperature determines the level of thermal support inside a cloud. Information about the gas temperature is thus a prerequisite for evaluating the importance of turbulence. Low mass cores have been found to have fairly uniform temperatures according to NH₃ observations (Tafalla et al. 2002). As modeled, this uniformity of temperature applies to regions of modest to large extinction, over which ammonia is observed. As such, it does not, for example, exclude the possibility of the edges of dark clouds being heated by the ISRF (Snell 1981; Young et al. 1982).

The temperature structure of massive cores is not well characterized. In this study we use the inversion transitions of NH₃ to probe the Orion core temperatures. In the remainder of this section we discuss the structure of the ammonia molecule and how we use it for determining the gas temperature. In Section 3 we present the observations, and in Section 4 we discuss the temperature structure that we obtain for the HMSF cores. We analyze the statistical uncertainties associated with the temperature gradients in Section 4.2. In Section 5 we present a model for the temperature distribution in these cores based on dust heating by the enhanced radiation field in the surrounding material. We discuss our findings and summarize our conclusions in Section 6.

2.1. Characteristics of Ammonia Inversion Transitions

Ammonia is a symmetric top molecule, which produces a relatively simple rotational energy level structure. The groups of levels having quantum number K , which describes

the angular momentum around the symmetry axis through the nitrogen atom, are called “ K -ladders”. Radiative transitions between K -ladders, such as (2,1) to (2,2) are prohibited. Therefore, the relative level population of the (2,2) and (1,1) levels is affected only by collisions. If the populations of levels in different K -ladders can be determined, their ratio will be a measure of their excitation, and thus of the temperature of the collision partners.

The positions of the energy levels are also helpful in determining the kinetic temperature. The metastable levels (lowest level in each K -ladder) (1,1) and (2,2) are at energies equivalent to 23 K and 64 K, respectively, above the ground state. At temperatures characteristic of GMCs, these levels will be significantly populated. Higher J levels, on the other hand, will be much less populated. The population of the (2,1) level, for example, will only be 7.6% of that of the (1,1) level in a cloud thermalized at 20 K. Thus, the metastable levels have most of the NH_3 molecules in each K -ladder at moderate temperatures.

Each metastable level for $K \neq 0$ is split into a pair of so-called inversion levels. The frequencies of inversion transitions of the (1,1) and (2,2) levels are very close, and their proximity proves to be a major convenience, since they can be observed simultaneously and their relative calibration is largely independent of antenna efficiency and pointing.

The inversion transitions are further split into hyperfine components due to the coupling between the nuclear spins of N and H and molecular rotation. As described by Rydbeck et al. (1977), there are 18 components in the (1,1) inversion transition. Usually the individual hyperfine transitions are not resolved and only five groups can be identified in a spectrum of an interstellar cloud. The relative strength of the main (m) component (the central group) and the satellite components (s) is determined theoretically under the assumption that they have the same level of excitation. For the (1,1) transition, the optical depths of the five groups conform to the following relations

$$\begin{aligned} \tau^m(1,1) &= 3.60\tau^s(1,1) \text{ (the two inner satellite components) ,} \\ \tau^m(1,1) &= 4.50\tau^s(1,1) \text{ (the two outer satellite components) ,} \\ \tau^m(1,1) &= 0.50\tau(1,1) \text{ ,} \end{aligned} \tag{3}$$

where τ , τ^m , and τ^s are the optical depths of the total, main line, and the individual satellite lines, respectively. For the (2,2) transition, since only the main line is typically visible, the relation of practical use is

$$\tau(2,2) = 1.26\tau^m(2,2) \text{ .} \tag{4}$$

2.2. Derivation of The Kinetic Temperature and NH₃ Column Density

For a cloud with temperature around 20 K and about 1 km s⁻¹ doppler broadened line width, we usually can detect the hyperfine components of the (1,1) transition in five groups but only the main component of the (2,2) transition.

A standard procedure to derive the kinetic temperature through such observations is discussed by Ho & Townes (1983). In this procedure, the main and the satellite antenna temperatures of the (1,1) line and the main antenna temperature of the (2,2) are obtained through fitting the spectra. These three quantities are then combined with equations (3) and (4) to derive the relative populations of the (2,2) and (1,1) levels, defined by the rotation temperature, denoted T_R . T_R can be converted to T_k through excitation calculations, most conveniently employing the three level approximation of Walmsley & Ungerechts (1983).

In our derivation, we follow the same line of argument discussed above, but incorporate two recent developments. First, the optical depths of the (1,1) and (2,2) transitions are not directly fitted in deriving T_R . We use the fitting scheme built into GILDAS, which chooses a rather particular set of parameters (Bachiller, Guilloteau & Kahane 1987). These parameters can be combined to give T_R under the same assumptions concerning uniform and equal excitation conditions, with this technique being more stable at low optical depths. The column density of the (1,1) level ($N(1,1)$), also a result of this fitting procedure, is used to calculate the total column density of NH₃ assuming that only the four lowest levels are populated, and that their relative populations are all defined by T_R , using (Rohlfs & Wilson 1996)

$$N(\text{NH}_3) = N(1,1) \left[\frac{1}{3} \exp(23.1/T_R) + 1 + \frac{5}{3} \exp(-41.2/T_R) + \frac{14}{3} \exp(-99.4/T_R) \right] . \quad (5)$$

The peak NH₃ column densities derived are listed in Table 1. Note that the higher metastable levels, such as (4,4), contain less than 1% of the total population.

Second, Danby et al. (1988) have calculated the cross sections for collisions between H₂ and NH₃ in states up to J=5. These authors also provide results of excitation analysis for graphically converting T_R to T_k . We have fitted a polynomial to their curve and use it instead of the analytic approximation of Walmsley & Ungerechts (1983).

The assumption of equal excitation, which underlies all the fitting procedures discussed above, will bring uncertainties into the derivation, especially in a low density environment. According to Stutzki & Winnewisser (1985), such effects are small for the derived rotational temperature under the conditions of the Orion cores ($n(\text{H}_2) \sim 5 \times 10^4 \text{ cm}^{-3}$). The uncertainty in T_k is dominated by the noise in the (2,2) spectra, as discussed in a later section.

The lower excitation of the satellite lines causes an underestimate of the column density

derived through equation (5) by about 10%. The exclusion of non-metastable levels introduces another $\sim 5\%$ underestimate. Based on the NH_3 column density, the C^{18}O column density (discussed in a later paper), and a constant C^{18}O abundance $[\text{C}^{18}\text{O}]/[\text{H}_2]=1.7 \times 10^{-7}$, we find the average NH_3 fractional abundance in the Orion cores to be 5×10^{-9} .

3. Observations

The majority of our ammonia data come from the Effelsberg 100m telescope. Calibration of the 100m is carried out by observations of point sources. The raw data are in system units, say counts, for which two factors are needed for the conversion to antenna temperature units. The first factor is ‘K/counts’, relating system units to antenna temperature. This is obtained using noise sources which have been calibrated against thermal loads. The second factor is ‘K/Jy’, which is given by the effective area divided by $2k$, with k being Boltzmann’s constant. This factor is obtained by observing point–source calibrators, including 3C147 (Ott et al. 1994). The limited data obtained using the NRAO ⁴ 140 foot telescope was also converted to antenna temperature using separately–calibrated noise diodes. The aperture efficiency was determined by observations of standard radio point sources.

Our Orion sources are not point sources relative to the beam, in which case the main beam efficiency ϵ_{mb} is more relevant than the aperture efficiency ϵ_A . For a known beam shape, ϵ_{mb} can be obtained from ϵ_A . The main beam solid angle, Ω_{mb} , defined as the integral over the main beam of the normalized power pattern, can be straightforwardly determined if a Gaussian satisfactorily represents the main beam. Thus, we find that $\Omega_{mb} = 1.13\theta_{FWHM}^2$, where θ_{FWHM} is the full width to half maximum beam width. The main beam efficiency is then obtained from

$$\epsilon_{mb} = \frac{\Omega_{mb}}{\Omega_A} = \frac{\Omega_{mb}A_p\epsilon_A}{\lambda^2}, \quad (6)$$

where Ω_A is the antenna solid angle, and we have used the antenna theorem to relate it to the effective area A_e , which is equal to the product of the physical area A_p and the aperture efficiency.

At the 140 foot telescope, we measured the beam efficiency to be about 20%. There is also evidence of dish deformation as the source elevation varies. For this reason, the data from the 140 foot are not calibrated for their absolute intensity. We used our 140 foot time to search for ammonia peaks in our Orion sources and obtained several kinetic temperature

⁴The National Radio Astronomy Observatory is a facility of the National Science Foundation operated under cooperative agreement by Associated Universities, Inc.

measurements, which are relatively independent of absolute calibration.

At Effelsberg, only the inner 75m of the 100m antenna is usable at 24 GHz, giving a FWHM beam size of $43''$. We determine the main beam efficiency to be around 0.60 and the data has been calibrated accordingly. However, atmospheric effects are not removed, and there were some gain variations (Muders 2001, private communication), so that the uncertainty can be as large as 50%.

The autocorrelator AK90, at Effelsberg, is divided into four quadrants, each with 2048 channels and 20MHz bandwidth. This bandwidth allows frequency switching even for the NH_3 hyperfine lines. The (1,1) and (2,2) inversion transitions are observed simultaneously in two linear polarizations, which are then averaged. The processed data have a velocity resolution of 0.24 km s^{-1} . With single beam pointings, we constructed beam-sampled maps at $0.738'$ spacing to cover the same region as the FCRAO observations. Maps were obtained of the sources ORI1, ORI2, ORI4 and ORI8 (Table 1).

4. Temperature and Turbulence Structure

4.1. Temperature Gradients

The (2,2) line intensity is usually less than 50% of the (1,1) intensity. Since the two inversion transitions are observed simultaneously, the signal to noise ratio (S/N) of a (2,2) spectrum is a factor of two lower than that of the corresponding (1,1) spectrum. As shown in the sample spectra map (Figure 1), the limiting factor on obtaining an accurate value of the kinetic temperature is the noise level in the (2,2) data.

We set a 5σ criterion, i.e., only those data whose (2,2) peak T_A is higher than $5 \times$ (*RMS Noise*) are used in derivation of kinetic temperature. Abiding by this standard, we obtained temperature maps of ORI1, ORI2, ORI4 and ORI8 (Figure 2). The kinetic temperatures at single points in ORI5 and ORI7 have also been determined (see Table 1). The angular offsets have been converted to distance using a distance of 480 pc to the Orion star molecular cloud (Genzel et al. 1991).

The kinetic temperatures at positions of peak integrated intensities of these sources range from 13 K to 19 K. These sources thus do represent a collection of cold, quiescent cloud cores as hoped for when developing the source selection criteria.

At the centers of these cores, the temperatures are generally lower than those toward the edge of the maps. This is natural for externally illuminated cores, as the heating from UV is reduced by the extinction, which should result in lower dust temperatures. In addition the

increased molecular density expected in these cores provides more cooling for the gas, and lower gas (kinetic) temperatures should result. In the Orion molecular cloud, the heating comes mostly from the enhanced interstellar radiation field, which can explain the higher temperatures (25 K \sim 30 K) observed outside of these dense molecular cores. In the above discussion, there are actually two conclusions drawn based on our NH₃ observations. First, the cores are cold. Second, this temperature variation is correlated with the distribution of material, in this case, represented by the integrated intensities. Are these results credible? We address the uncertainties of our results in the following Section.

4.2. Statistical Analysis of Correlations between Temperature and Intensity

If the noise distribution is known, we can estimate the uncertainty of a particular parameter fitted to a spectrum. In most of our data, the noise in individual channels is uncorrelated (between channels) Gaussian noise. The functions being fitted to the spectra are usually either polynomials or Gaussians. Thus, it is easy to obtain the statistical uncertainty of a quantity such as the line strength T_A . The uncertainty in a particular parameter is usually given in combination with the quality of the data, σ , where σ is defined for Gaussian noise through $P(x) = \frac{1}{\sqrt{2\pi}\sigma} e^{-x^2/(2\sigma^2)}$ with $P(x)$ being the probability density function of the noise amplitude x and the mean noise amplitude being zero. σ is also called the RMS (root mean square) variation. The full width to half maximum (FWHM) of the Gaussian function is $\sqrt{8 \ln 2}\sigma$. Subtracting the fitted function from the data, we measure the σ from the residual noise so that we can make a statement about the line strength, such as T_A being at 3σ level.

Such statements, however, do not usually have direct physical meaning. For example, as discussed in the previous sections on deriving the kinetic temperature, two fitted quantities, one from a NH₃ (1,1) spectrum and the other from a NH₃ (2,2) spectrum, are combined to derive the rotational temperature. Then, through excitation calculations, the rotational temperature is converted to the kinetic temperature. What concerns us is the level of uncertainty in the kinetic temperature resulting from the noise in the original (1,1) and (2,2) spectra. An analytic solution through error propagation is not practical since the derivation involves integration, interpolation, and complicated functions.

We have devised an empirical approach to determine the uncertainty in the kinetic temperature, which is based on adding random noise to a perfect spectrum and using it to derive the kinetic temperature. By repeating this experiment many times, each with independently generated noise, we obtain an ensemble of spectra, each of which is associated with a specific T_k through the fitting procedure. Since the added noise in each spectrum is independent, each determined T_k can be treated as an independent representation of a random variable.

According to the central limit theorem, a Gaussian describes the distribution of kinetic temperatures regardless of the intrinsic distribution of T_k with respect to noise magnitude.

Figure 3 illustrates how noisy spectra are constructed by adding Gaussian noise (Figure 4) to a ‘perfect’ spectrum. The ‘perfect’ spectra are obtained by averaging over our maps, and thus have negligible noise. The RMS level of 0.01 K is a typical value achieved in our observations at Effelsberg. ‘Perfect’ spectra are so scaled that the (2,2) peak is at a certain signal to noise ratio, e.g. 5σ or 10σ .

The uncertainty in T_k depends not only on the noise σ , but also on the signal strength. A better fit with less spread can be achieved at a higher signal to noise ratio. The results of our ‘noise’ experiment (Figure 5) are consistent with this expectation. The kinetic temperatures obtained through the simulation are consistent with a Gaussian distribution. At the 5σ level, which is our criterion for attempting any temperature calculation, the RMS of the T_k distribution is 1.8 K. At the 10σ level, which is a typical S/N for data around the cloud centers, the RMS is 0.9 K. In between, the RMS of the derived T_k goes down roughly linearly as a function of the S/N (Figure 6). The dependence of the RMS of the fitted T_k on the S/N ratio of the original spectra is well described by

$$RMS(K) = -0.15 + \frac{10.3}{S/N} + 0.01(S/N) , \quad (7)$$

which is used to assign uncertainties to individual data points when needed. This numerical fit is applicable only to a reasonable range (3 to 20) of the signal to noise ratio.

Such a noise distribution, obtained through appropriate simulations, enables us to make meaningful statements about kinetic temperatures. For example, at the center of ORI1, $T_k = 19 \pm 0.9$ K at a 67% confidence level and at the edge of ORI1, $T_k = 25 \pm 1.8$ K at a 67% confidence level. With the uncertainties of the derived T_k known, we can tackle the problem of assessing the validity of the temperature gradients and their dependence on core column density, as discussed earlier.

First, we examine the claim that there are significant temperature variations within the maps. The mapping data of T_k (Figure 2) can be divided into two groups according to the integrated intensity at each point. The central group includes those data points whose intensity is higher than half of the peak value of each map, i.e., the points within the dotted contour line of integrated intensity in Figure 2. The edge group includes all other points.

The mean T_k in each map is subtracted from the data points in our sample. Thus, we have four maps of temperature variations, all with zero mean. We can combine them into one combined sample including 85 points, out of which 54 are in the edge group and 31 are in the central group. The mean of edge group is 0.76 K and that of the central group is

-1.3 K. On average, the temperature in central regions is 2.1 Kelvin lower than that on the outside.

To evaluate the significance regarding the difference of means (\bar{A} and \bar{B}) of two samples (A and B), we use Student's t test, whose relevant statistic is

$$t = \frac{\bar{A} - \bar{B}}{(\Delta A/N_A + \Delta B/N_B)^{1/2}} , \quad (8)$$

where ΔA is the variance of sample A , N_A is the number of points in sample A , and ΔB and N_B are these quantities for sample B . If the distribution is known to be a Gaussian, Δ is equal to σ^2 . In our case, the variance is 0.81 K and 3.2 K for the central group and the edge group, respectively. Note that the two groups have different variances due to different S/N of the NH_3 spectra. Using Student's t test on samples with different variances may be troubling, but not for cases where both distributions are known to be Gaussian.

The number of degrees of freedom for Student's t distribution in this problem is

$$\nu = \frac{(\Delta A/N_A + \Delta B/N_B)^2}{\frac{(\Delta A/N_A)^2}{N_A-1} + \frac{(\Delta B/N_B)^2}{N_B-1}} . \quad (9)$$

For two samples having equal mean values, the probability with which the difference in means would be just this large or larger by chance, is calculated from Student's distribution using

$$p(\text{null}) = I_{\frac{\nu}{\nu+1}}(\nu/2, 1/2) , \quad (10)$$

where I is the incomplete beta function (see e.g. Press et al. 1988). Applying equations (8), (9) and (10), we obtain $p(\text{null})$ to be 1.1×10^{-9} . The null hypothesis is very unlikely: the temperatures in central regions of the dense cores studied here are statistically significantly lower than in the outer regions.

Now let us consider the second claim raised in the previous section concerning the correlation between intensity and temperature. For pairs of quantities (T_k^i, T_{int}^i) , $i = 1, 2, \dots, N$, the most commonly used linear correlation coefficient is called Pearson's r , given by

$$r = \frac{\sum_i (T_k^i - \bar{T}_k)(T_{int}^i - \bar{T}_{int})}{\sqrt{\sum_i (T_k^i - \bar{T}_k)^2} \sqrt{\sum_i (T_{int}^i - \bar{T}_{int})^2}} . \quad (11)$$

r ranges from -1 to 1 and indicates the level of correlation. But more important is the confidence level of any derived r . Even when the number of data pairs is not very large, as is the case here, the statistic

$$t = r \sqrt{\frac{N-2}{1-r^2}} \quad (12)$$

is still distributed like Student’s t-distribution in the null case (no correlation). The significance level of the null hypothesis is thus given by $p(\text{null})$ (Eq. 10). We calculate r and p for the four temperature/intensity maps of Orion cores. The results are given in Figure 7.

For ORI1, the anti-correlation between T_k and T_{int} is clear in the sense that the probability for two uncorrelated samples producing the same r by chance is as small as 0.01%. A similar statement can be made for ORI2 and ORI4. In ORI8, the probability of 30% is not very small for the null hypothesis. This is probably due to the combination of the larger size of the core with the limited size of our NH_3 map, which does not extend far enough to include outer regions with higher T_k .

4.3. Turbulence

With the knowledge of kinetic temperature, the turbulence in these cores can be quantified in terms of the nonthermal linewidth

$$\Delta V_{nt} = \sqrt{\Delta V^2 - \frac{8 \ln(2) k T_k}{\mu m_H}}, \quad (13)$$

where ΔV is the observed FWHM of the line, μ is the molecular weight, m_H is the hydrogen mass and k is Boltzmann’s constant. To compare it more directly with the thermal motion, we define

$$T_{nt} = \frac{\mu m_H}{8 \ln(2) k} \Delta V^2 - T_k. \quad (14)$$

T_{nt} measures ΔV_{nt} in Kelvins. The correlation between the integrated intensities and the turbulence is presented in Figure 8. The combined effect of uncertainties in T_k and ΔV amounts to about a 5 K 1σ uncertainty in T_{nt} .

The values of T_{nt} range from 100 to 1000 K. Compared to 10 to 20 K for T_K , there is no doubt that these clouds are dominated by turbulence throughout. This is in contrast with some dark cloud cores, which approach being thermalized toward the center (Goodman et al. 1998). Three (ORI1, ORI2, ORI4) out of four sources exhibit an anticorrelation between turbulence and intensity. For ORI8, there is no apparent correlation. This is similar to the relations we find for T_k . Again, we may not have enough data on the outer portions, where the emission is weaker.

In this section, we have presented evidence that these massive cores in Orion are generally colder inside. They are supersonic, with turbulence diminishing toward the center of three of the four cores.

5. Thermal Balance of Externally Heated Cores

The massive quiescent cores of this study are warmer than molecular regions away from regions of star-formation and shielded from the interstellar radiation field (ISRF), which have characteristic temperatures $\simeq 10$ K. Thus, there must be additional heating sources present. The kinetic temperatures we are considering here come from observations of NH_3 , which as seen in previous sections, is well-confined to limited regions within the much larger L1640 and L1641 portions of the Orion molecular cloud. As such, we are measuring the temperature in regions with considerable extinction, which are plausibly quite different than the outer parts of the general molecular material. The general picture of the Orion molecular cloud/HII region is that the “front” of the cloud, the side facing the Earth, is heated by the radiation from the Trapezium star cluster, located yet closer to us. This is the basis for the model of Stacey et al. (1993) for the distribution of ionizing radiation across the surface of the cloud, which is responsible for the very extended [CII] emission. The FUV intensity at the interface between the molecular cloud and the Trapezium is estimated by these authors to be a factor 5×10^4 greater than that of the nominal ISRF.

In addition, there will be some heating by the embedded sources. For example, Strom, Strom, & Merrill (1993) found $\simeq 1500$ solar-type PMS stars distributed throughout the L1641 molecular cloud. The region they studied extends over a much larger region than that defined by the present sample of massive cores. This suggests that the heating from embedded PMS stars as well as from outflows (Morgan et al. 1991), while locally possibly significant, is certainly very inhomogeneous, and in aggregate is not very important. Thus we will analyze the thermal structure of the cores considering only the diffuse heating from the Trapezium stars.

Following the treatment of Stacey et al. (1993), we take the Trapezium stars to be located $d_o = 0.39$ pc in front of the surface of the molecular cloud, which is assumed to be a plane. Then, the radiation field normalized to the standard ISRF at a projected distance d_p (in pc parallel to the cloud surface) from the Trapezium to the point of interest is given by

$$\chi = \frac{8.6 \times 10^3}{(d_o^2 + d_p^2)^{3/2}} . \quad (15)$$

For ORI1, $d_p = 3.2$ pc and $\chi = 260$, for ORI2, $d_p = 4.8$ pc and $\chi = 77$, for ORI4, $d_p = 7.1$ pc and $\chi = 24$, and for ORI8, $d_p = 9.1$ pc and $\chi = 11$. These are upper limits, due to 1) the intervening absorption of the radiation between the Trapezium and the molecular cloud, and 2) the absorption in the molecular cloud itself. Both of these are quite uncertain, particularly as the location of the cores relative to the surface of the molecular cloud is not

known. We thus consider cores with a range of values of χ ⁵

We have used the radiative transfer code DUSTY (Ivezić, Nenkova, & Elitzur 1999) to calculate the dust temperature within a spherical core having specified value of χ on its periphery. The form of the external ISRF is given by Mathis, Mezger, & Panagia (1983) for a Galactrocentric distance of 10 kpc. The dust density is uniform throughout the core, and the dust properties are those of Draine & Lee (1984) with relative number densities 0.53 silicate and 0.47 graphite grains. The grain size distribution is given by a power law of index $q = 3.5$ as discussed by Mathis, Ruml, & Nordsieck (1977), with a minimum grain radius $a_{min} = 0.005 \mu\text{m}$, and maximum grain radius $a_{max} = 0.25 \mu\text{m}$.

The code carries out calculations on a grid of optical depth at reference wavelength λ_0 specified to be $0.55 \mu\text{m}$. In the upper panel of Figure 9, we show the dust temperature as a function of the optical depth in the visible $\tau_v(\lambda_0)$. These calculations are all for a cloud having τ_v from edge to center equal to 10 (this is somewhat less than for the massive cloud cores of interest here, but the behavior is the same). We see that the dust temperature is enhanced at the edge of the core, but drops significantly when the optical depth to the edge is a few, and reaches an asymptotic value for optical depths greater than this.

The dust temperature exhibits a very clear variation as a function of ISRF intensity, both at the core edge, and at its center. In Figure 10, we show the variation in dust temperature as a function of χ , for $\tau_v = 0$ and 10. In both cases, the slope of the log–log straight line indicates that $T_{dust} \propto \chi^{1/6}$. This is consistent with simplest dust thermal balance consideration, with dust cooling varying as T_{dust}^6 and dust heating being proportional to χ . This cooling law is what is expected if the dust emissivity throughout the wavelength range of interest varies as ν^2 (Goldsmith 2001). While the dust emissivity in the Draine & Lee (1984) model does not obey this law exactly throughout the millimeter–to–infrared range, it is sufficiently close at these modest temperatures that the cooling variation is very accurately represented by a T_{dust}^6 power law.

It is reasonable that the dust heating should be proportional to χ for small τ_v , but it is somewhat surprising that this continues when the optical depth between the external heating source and the dust is much greater than unity. This can be understood, however,

⁵The “standard” ISRF of Mathis, Mezger, & Panagia (1983) (MMP) has been reexamined by Black (1994) who finds a modest factor greater flux at infrared – far infrared wavelengths. The difference in the dust temperature that would result is small for $\chi = 1$. In models of spherical dust clouds by Evans et al. (2001), the corresponding difference is 2.5 K at the cloud center, and even less at the outside of the cloud. A similar calculation by Zucconi, Walmsley, & Galli (2001) gives a difference of about 1 K. The modeling here is necessarily relatively crude given the uncertainties in geometry and internal extinction, so that using the MMP radiation field and multiplicative factor χ is a reasonable procedure.

as a consequence of the heating of the dust by radiation emitted by other dust grains in the cloud. The total heating of a grain at the cloud center still varies in proportion to χ even though the wavelengths at which the heating occurs are much longer than for direct heating by the ISRF at low optical depth.

The exact values of the dust heating and hence the dust temperature depend on the total optical depth of the core as well as the optical depth to the core edge. This is seen in the lower panel of Figure 9, which shows the variation in dust temperature for $\chi = 100$, as a function of τ_v , for three clouds having different values of central optical depth τ_c . As expected, the dust temperature is independent of τ_c for small values of τ_v , since the heating is dominated by direct input from the ISRF. As the dust heating makes a transition to being dominated by reradiation from other dust grains in the core, we see a systematic effect, which is that the dust temperature decreases as the central optical depth τ_c increases. Thus, a more opaque cloud is characterized by cooler dust in its interior. This can be seen to be a result of balance between total cooling of the cloud, which (for its interior) is dominated by emission at relatively long wavelengths, which will not be highly optically thick. If we consider two clouds of the same size, they intercept the same total energy from the ISRF, so that total heating is the same. The cooling will, however, be greater for the cloud of higher opacity, since it will radiate with greater or equal efficiency at all wavelengths, and thus the dust temperature within it will be lower.

Thus, while we can use simple scaling rules to determine dust temperature variation as a function of χ , the exact value of T_{dust} depends on position in the core and the total optical depth of the core. From column 7 of Table 1, we see that the $C^{18}O$ column densities for the four cores studied in detail (ORI1, ORI2, ORI4, and ORI8) are in the range $\simeq 5 - 13 \times 10^{15} \text{ cm}^{-2}$, which for a canonical fractional abundance $X(C^{18}O) = 10^{-7}$ and with $\tau_v = 10^{-21}N(H_2)$ implies edge-to-center visual optical depths (τ_c) between 25 and 65. Using $\tau_c = 31.6$ as a representative value, we find that the dust temperature, T_d , at the edge and center, respectively, are 26 K and 12 K for $\chi = 10$, 38 K and 29 K for $\chi = 100$, and 56 K and 28 K for $\chi = 1000$.

The gas temperature, T_g , is affected by a variety of processes. In the well-shielded centers of these cores, the primary effects are cosmic ray heating, molecular line cooling and collisional heating due to dust-gas collisions. Using the parameters from Goldsmith (2001) with no depletion, for $T_d = 20$ K, we find that $T_g = 13.5$ K for $n(H_2) = 10^4 \text{ cm}^{-3}$ and 18 K for $n(H_2) = 10^5 \text{ cm}^{-3}$. Thus, given the molecular hydrogen densities for these cores, $\simeq 4 - 20 \times 10^4 \text{ cm}^{-3}$, the central gas temperature, which is the kinetic temperature determined from the NH_3 observations, should be a few K lower than the dust temperature. The situation at the edges of the cores is more complicated, as the fractional abundance of molecular coolants

will drop, while the abundances of atomic and ionic coolants will increase. The density may also plausibly be lower, although the degree of central condensation of these cores has not been determined.

Comparison of observational results of core “central” temperatures from our NH_3 data with the expectations from external dust heating shows reasonable agreement. For ORI1, ORI2, and ORI4, the kinetic temperature is 2 – 4 K below that expected for the dust, which is consistent with the thermal balance models and core densities (Table 1). For ORI8, the kinetic temperature is a few K higher than the dust temperature predicted by the model. The data for this source are the least extensive of the mapped cores, but the central portion does appear to be well defined (see Figure 2). It is possible that some other modest heating source is raising the temperature of this core.

The “external” core temperatures found by Wilson et al. (1999) are in surprisingly good agreement with the dust temperature predicted from heating by the Trapezium. It is plausible that the ^{12}CO samples the temperature in a relatively thin shell at the periphery of the core. This can be seen from evaluating the standard expression for the optical depth, which for $T_k = 20$ K and $n(\text{H}_2) = 10^3 \text{ cm}^{-3}$, yields for ^{12}CO with a Gaussian line profile having FWHM $\delta v \text{ km s}^{-1}$

$$\tau_{1,0}(^{12}\text{CO}) = 5.5 \times 10^{-17} \frac{N(^{12}\text{CO})/\text{cm}^{-2}}{\delta v/\text{km s}^{-1}} . \quad (16)$$

For a nominal fractional abundance, $N(^{12}\text{CO}) = 10^{-4}N(\text{H}_2) = 10^{17}\tau_v$. Substituting this in the preceding equation, we see that for a FWHM line width equal to 2 km s^{-1} ,

$$\tau_{1,0}(^{12}\text{CO}) \simeq 3\tau_v . \quad (17)$$

The optical depth of the $J = 2-1$ transition under these same conditions is a factor of 2.6 greater than that of the $1-0$ transition, and $\tau_{3,2} = 3\tau_{1,0}$. Thus, if a fractional abundance $X(^{12}\text{CO}) = 10^{-4}$ prevails right to the edge of the cloud, the ^{12}CO rotational transitions become optically thick in a small fraction of the thickness required to have a dust optical depth of unity in the visible. However, the fractional abundance of ^{12}CO drops in the outer portion of the core due to photodestruction, and despite its own self-shielding, its fractional abundance becomes significant only when τ_v approaches unity. In any case, it appears secure that the $J = 3-2$ transition of ^{12}CO as observed by Wilson et al. (1999) will probe the gas temperature in the outer layer of the core. The density there may be inadequate for perfect collisional gas-dust coupling, but other processes, including photoelectric heating, will help raise the gas temperature. Thus, although the close agreement between the dust temperature predicted by the external heating models, and the temperature derived from $J = 3-2$ ^{12}CO

observations may be somewhat fortuitous, it appears that we can use the temperature from ^{12}CO as a probe of the outer region of the core ⁶.

Overall, the temperatures known from CO and NH_3 observations can be well explained by the dust being heated by an enhanced external UV field.

6. Summary and Discussion

In this paper we have presented the first portion of the results of a study of dense cores in the nearby Orion Giant Molecular Cloud. The cores selected are apparently free of signposts of star formation (embedded sources or outflows) and which are relatively distant from the perturbing effects of the formation of massive stars. We have focused on the temperature structure of these cores, primarily as traced by NH_3 . We have also utilized other parameters obtained from mapping in C^{18}O , which will be presented in detail elsewhere. In particular, the mean density of the cores is $\simeq 4 - 20 \times 10^4 \text{ cm}^{-3}$. This is significantly higher than the mean density of the molecular cloud at these large distances ($\simeq 20'$ to $90'$; $\simeq 4$ to 14 pc) from its center ⁷. The density contrast between these cores and the surrounding material is at least an order of magnitude.

We have discussed in some detail the issue of the temperature structure of these cores. They appear as significantly cooler than the surrounding material. This is seen in two different ways. First, the kinetic temperature derived from the NH_3 (1,1) and (2,2) lines drops from the edges to the centers of the cores. Their central temperatures are between 14

⁶The issue of externally heated material in GMCs, particularly Orion, is not new, but is not always recognized in analyses of multi-transition studies and maps. Castets et al. (1990) inferred that the molecular gas in Orion is hotter on the outside than in its interior, based on arguments from densities obtained from the two lowest transitions of ^{13}CO , in a manner similar to that found for dark clouds by Young et al. (1982). Tauber & Goldsmith (1990) found that their observations of a ratio $^{12}\text{CO } J = 3-2$ to $J = 1-0 \simeq 1.4$ could be reproduced by hot-edged clumps. Gierens, Stutzki, & Winnewisser (1992) developed a detailed model of CO emission from a clump with photoelectric heating by a strong external radiation field, and find that this can satisfactorily reproduce the observations of Castets et al. (1990). The ^{12}CO emission reflects the $\simeq 30 \text{ K}$ temperature at the inner edge of the PDR bounding the molecular portion of the clump. This is considerably warmer than the interior of the clump, which contributes significantly to the ^{13}CO emission.

⁷Multitransition determinations of densities have yielded comparable or higher values over regions extending $\leq 10'$ from the cloud center (Bergin, Snell, & Goldsmith 1996). However, comparison of these densities with those obtained from virial arguments (Goldsmith 1999) reinforces the picture that there is a filling factor of high density material which is relatively large near the center of the GMC, but drops significantly at larger distances (Mundy et al. 1986). At the distances from the Trapezium of the cores studied here, the average cloud density is $n(\text{H}_2) \simeq \text{few} \times 10^3 \text{ cm}^{-3}$.

and 19 K, for the four cores studied in greatest detail. The core edges are between 4 and 8 K warmer than the centers. The ability to probe the core temperature structure solely with NH_3 is limited by the dramatic decrease in its emission as a function of increasing distance from the core center. Second, we can get a better picture of the overall thermal structure by including the kinetic temperature derived from ^{12}CO , which samples an outer “onion skin” of the core. Using $J = 3 - 2$ data from the literature, we find temperatures between 18 and 33 K. This is consistent with model calculations of dust heating by a single source, the Trapezium, the radiative transfer within the dust of the core, and dust–gas coupling via collisions.

These cores, although colder than their surroundings, are still supersonic. They are more quiescent than their surroundings with turbulence level dropping toward the center, as indicated by the reduced nonthermal width of the NH_3 emission lines. Since the kinetic temperature has been derived independent of linewidth, this result has been established with confidence. This first part of a study of dense cores in HMSF molecular clouds has established some important parameters of these potential sites of star formation. The data and analysis presented in a subsequent paper will address the density, structure, and energetics of these regions, confirming them as plausible, relatively isolated sites of future formation of high mass stars.

We thank P. Schilke and D. Muders for their kind help with the telescope operation and data calibration of the Effelsberg 100–meter telescope. Our NH_3 observations were the last K–band undertaking at the 140–foot telescope, and they were only made possible with assistance from D. Balseer. The National Astronomy and Ionosphere Center is operated by Cornell University under a Cooperative Agreement with the National Science Foundation. The Five College Radio Astronomy Observatory is supported by NSF grant AST97-25951.

REFERENCES

- Benson, P. J. & Myers, P. C. 1989, *ApJS*, 71, 89
- Bachiller, R., Guilloteau, S., & Kahane, C. 1987, *A&A*, 173, 324
- Basu, S. & Mouschovias, T. C. 1995, *ApJ*, 453, 271
- Bergin, E.A., Snell, R.L., & Goldsmith, P.F. 1996, *ApJ*, 460, 343
- Black, J. 1994, in *ASP Conf. Ser. 58, The First Symposium on the Infrared Cirrus and Diffuse Interstellar Clouds*, ed. R.M. Cutri & W.B. Latter (San Francisco: ASP), 335

- Castets, A., Duvert, G., Dutrey, A., Bally, J., Langer, W.D., & Wilson, R.W. 1990, *A&A*, 234, 469
- Clayton, D. D. 1983, *Principles of Stellar Evolution and Nucleosynthesis*, (Chicago: University of Chicago Press), 470
- Clemens, D. P. & Barvainis, R. 1988, *ApJS*, 68, 257
- Danby, G., Flower, D. R., Valiron, P., Schilke, P., & Walmsley, C. M. 1988, *MNRAS*, 235, 229
- Draine, B.T. & Lee, H.M. 1984, *ApJ*, 285, 89
- Evans, N.J. II, Rawlings, J.M.C., Shirley, Y.L., & Mundy, L.G. 2001, *ApJ*557, 193
- Genzel, R., Watson, D.M., Crawford, M.K, & Townes, C.H. 1981, *ApJ*, 296, 766
- Gierens, K.M., Stutzki, J., & Winnewisser, G. 1992, *A&A*, 259, 271
- Goldsmith, P.F. 1999, in *Millimeter-Wave Astronomy: Molecular Chemistry & Physics in Space*, ed. W.F. Wall et al. (Dordrecht: Kluwer), 57
- Goldsmith, P.F. 2001, *ApJ*, 557, 736
- Goodman, A. A., Barranco, J. A., Wilner, D. J., & Heyer, M. H. 1998, *ApJ*, 504, 223
- Hillenbrand, L. A. & Hartmann, L. W. 1998, *ApJ*, 492, 540
- Ho, P. T. P. & Townes, C. H. 1983, *ARA&A*, 21, 239
- Ivezić, Ž., Nenkova, M., & Elitzur, M. 1999, *User Manual for DUSTY*, University of Kentucky Internal Report, accessible at <http://www.pa.uky.edu/~moshe/dusty>
- Jones, B. F. & Walker, M. F. 1988, *AJ*, 95, 1755
- Larson, R. B. 1969, *MNRAS*, 145, 271
- Mathis, J.S., Ruml, W., & Nordsieck, K.H. 1977, *ApJ*, 217, 425
- Mathis, J.S., Mezger, P.G., & Panagia, N. 1983, *A&A*, 128, 212
- Morgan, J.A., Schloerb, F.P., Snell, R.L., & Bally, J. 1991, *ApJ*, 376, 618
- Muench, A. A., Lada, E., Lada, C. J., & Alves, J. 2002, *ApJ*, 573, 366
- Mundy, L.G., Snell, R.L., Evans, N.J. II, Goldsmith, P.F., & Bally, J. 1986, *ApJ*, 306, 670

- Myers, P. C. & Goodman, A. A. 1988, *ApJ*, 329, 392
- Nakano, T. 1998, *ApJ*, 494, 587
- Onishi, T., Mizuno, A., Kawamura, A., Ogawa, H. & Fukui, Y. 1998, *ApJ*, 502, 296
- Penston, M. V. 1969, *MNRAS*, 144, 425
- Press, W. H., Flannery, B. P., Teukolsky, S. A. & Vetterling, W. T. 1988, *Numerical Recipes in C* (Cambridge: Cambridge University Press)
- Ott, M., Witzel, A., Quirrenbach, A., Krichbaum, T. P., Standke, K. J., Schalinski, C. J., & Hummel, C. A. 1994, *A&A*, 284, 331
- Rohlfs, K. & Wilson, T. L. 1996, *Tools of Radio Astronomy* (Berlin: Springer-Verlag Berlin), 368
- Rydbeck, O. E. H., Sume, A., Hjalmarsen, A., Ellder, J., Ronnang, B. O., & Kollberg, E. 1977, *ApJ*, 215, L35
- Shu, F. H. 1977, *ApJ*, 214, 488
- Shu, F. H., Adams, F. C. & Lizano, S. 1987, *ARA&A*, 25, 23
- Snell, R.L. 1981, *ApJS*, 45, 121
- Stacey, G. J., Jaffe, D. T., Geis, N., Grenzel, R., Harris, A. I., Poglitsch, A., Stutzki, J., & Townes, C. H. 1993, *ApJ*, 404, 219
- Strom, K.M., Strom, S.E., & Merrill, K.M. 1993, *ApJ*, 412, 233
- Stutzki, J. & Winnewisser, G. 1985, *A&A*, 148, 254
- Tafalla, M., Myers, P. C., Caselli, P., Walmsley, C. M., & Comito, C. 2002, *ApJ*, 569, 815
- Tatematsu, K.I., et al. 1993, *ApJ*, 404, 643
- Tauber, J.A. & Goldsmith, P.F. 1990, *ApJ*, 356, L63
- Walmsley, C. M. & Ungerechts, H. 1983, *A&A*, 122, 164
- Walmsley, M. 1995, in *Revista Mexicana de Astronomia y Astrofisica Conference Series*, Vol. 1, *Circumstellar Disks, Outflows, and Star Formation*, 137
- Wilson, T. L., Mauersberger, R., Gensheimer, P. D., Muders, D., & Bieging, J. H. 1999, *ApJ*, 525, 343

Wiseman, J. J. & Ho, P. T. P. 1998, *ApJ*, 502, 676

Ungerechts, H. & Thaddeus, P. 1987, *ApJS*, 63, 645

Young, J.S., Goldsmith, P.F., Langer, W.D., Wilson, R.W., & Carlson, E.R. 1982, *ApJ*, 261, 513

Yun, J. L. & Clemens, D. P. 1990, *ApJ*, 365, L73

Zucconi, A., Walmsley, C.M., & Galli, D. 2001, *A&A*, 376, 650

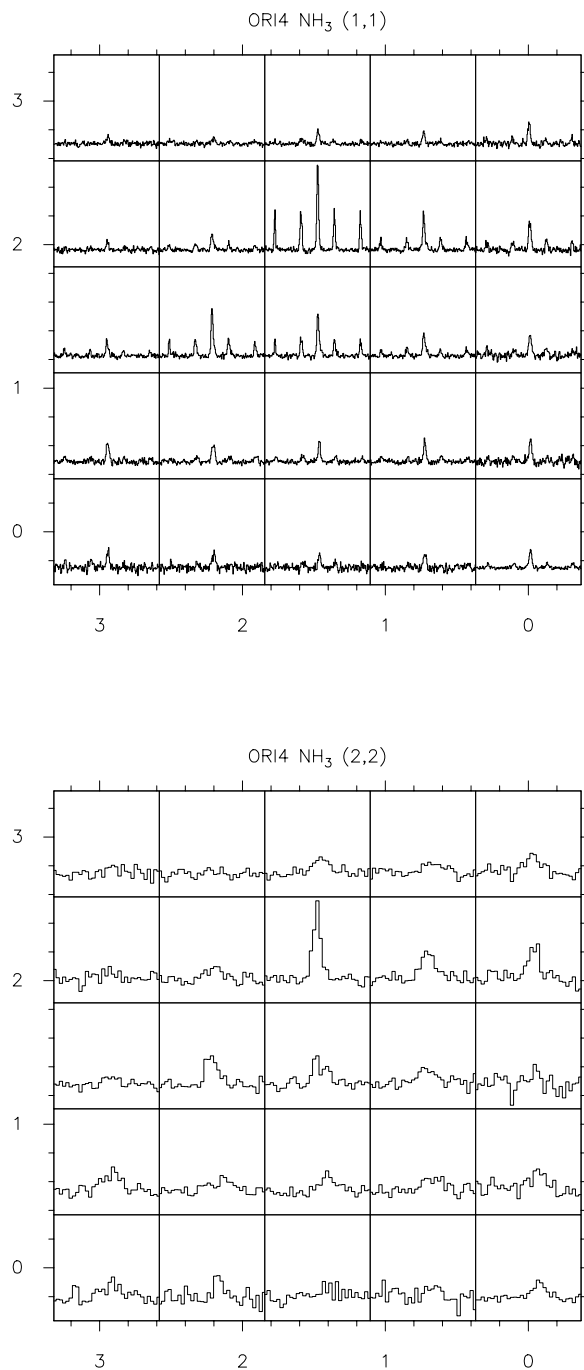


Fig. 1.— Arrays of NH₃ spectra of ORI4 at corresponding spatial offsets, given in units of minutes of arc from the central position (Table 1). Upper panel: (1,1) spectra plotted within the velocity range -16 to 32 km s⁻¹ and the antenna temperature range in the range -0.11 to 0.58 K. Lower panel: (2,2) spectra plotted within the velocity range 4 to 12 km s⁻¹ and the antenna temperature in the range -0.06 to 0.21 K.

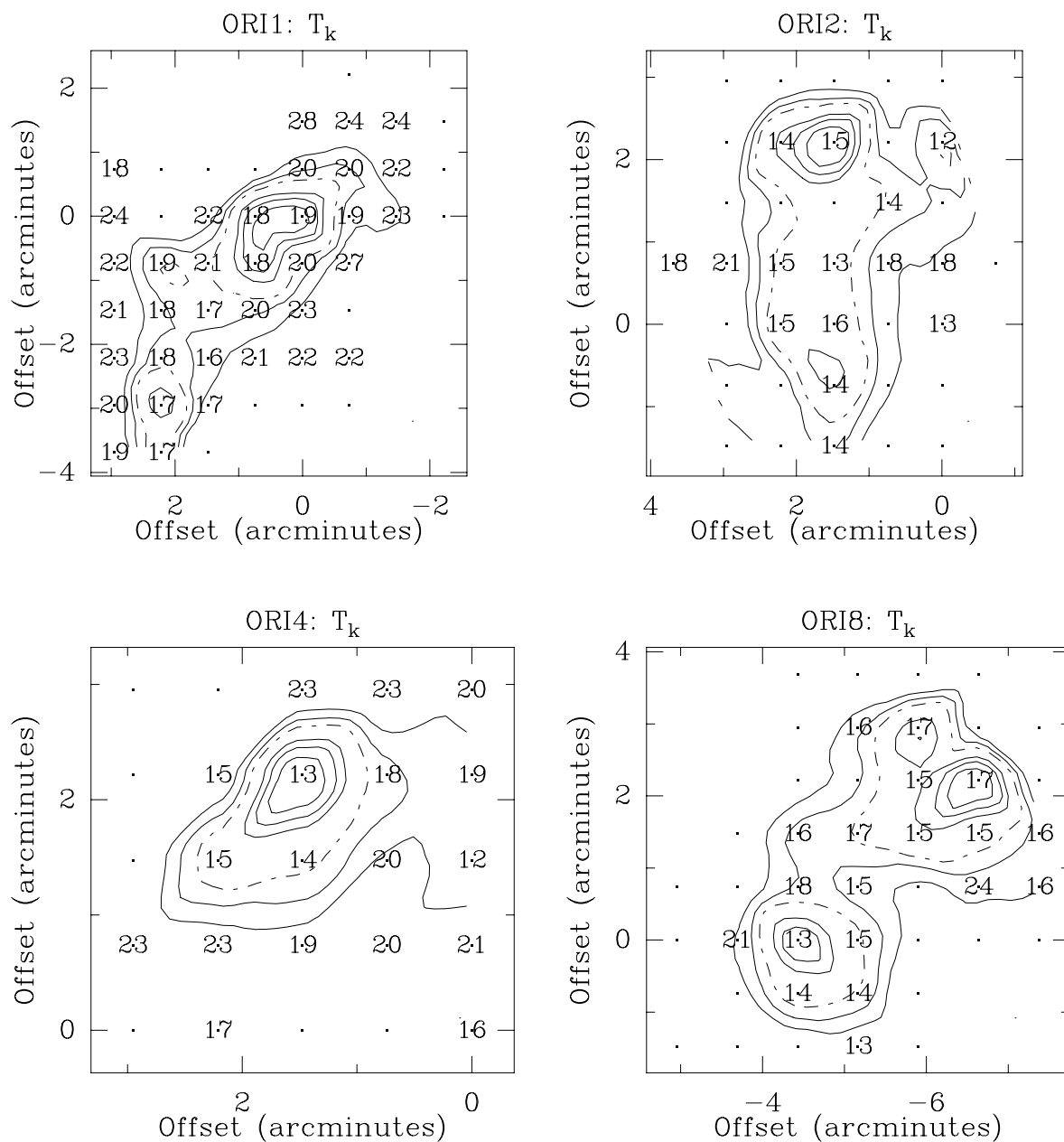


Fig. 2.— Derived kinetic temperatures overlaid with contours of the integrated intensity of the NH_3 (1,1) transition. The offset is given in arcminutes relative to center positions given in Table 1. The contour levels are at 0.3, 0.4, 0.5, 0.7, 0.8, and 0.9 times the peak value. The 0.5 contour is indicated by dashed lines. The dots indicate the positions where data have been obtained.

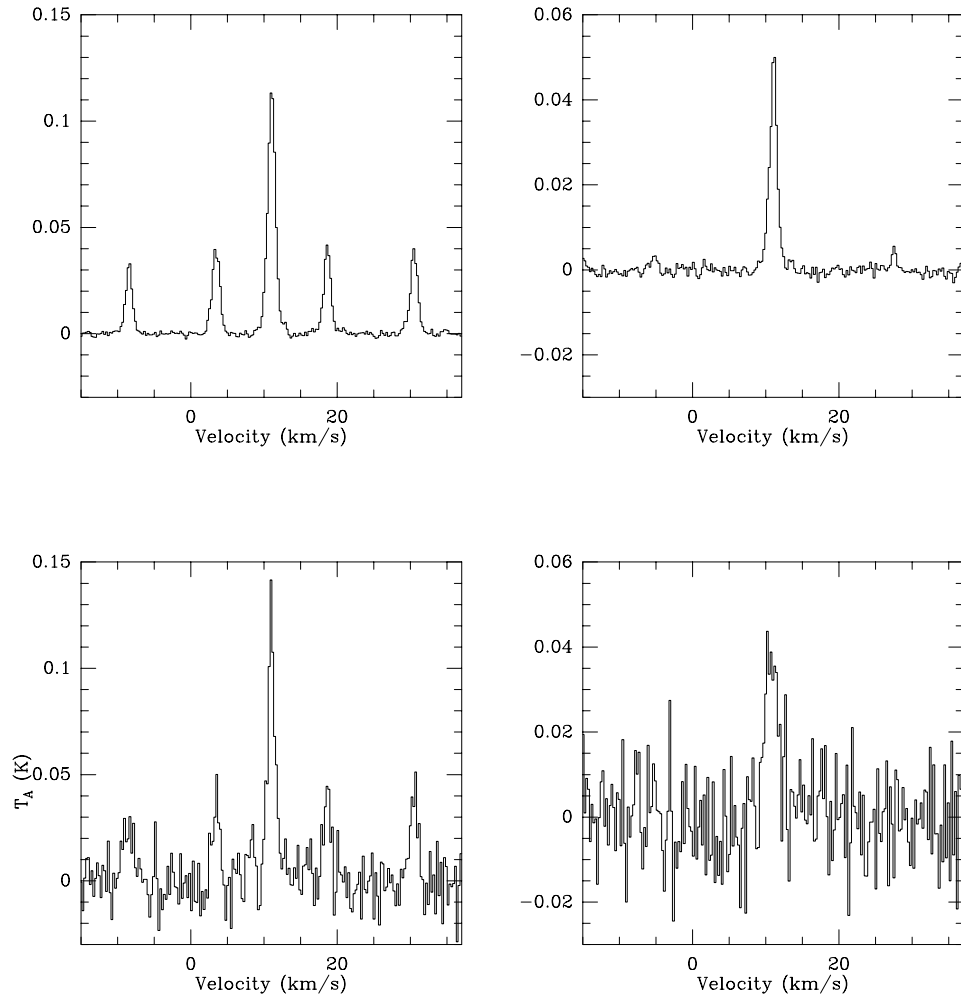


Fig. 3.— ‘Perfect’ spectra of NH_3 (upper panels) with added noise (lower panels). The (1,1) spectra are shown on the left and the (2,2) spectra on the right. The noise is Gaussian with 0.01 K RMS, which makes the Gaussian fit to the (2,2) spectrum significant at about the 5 σ level.

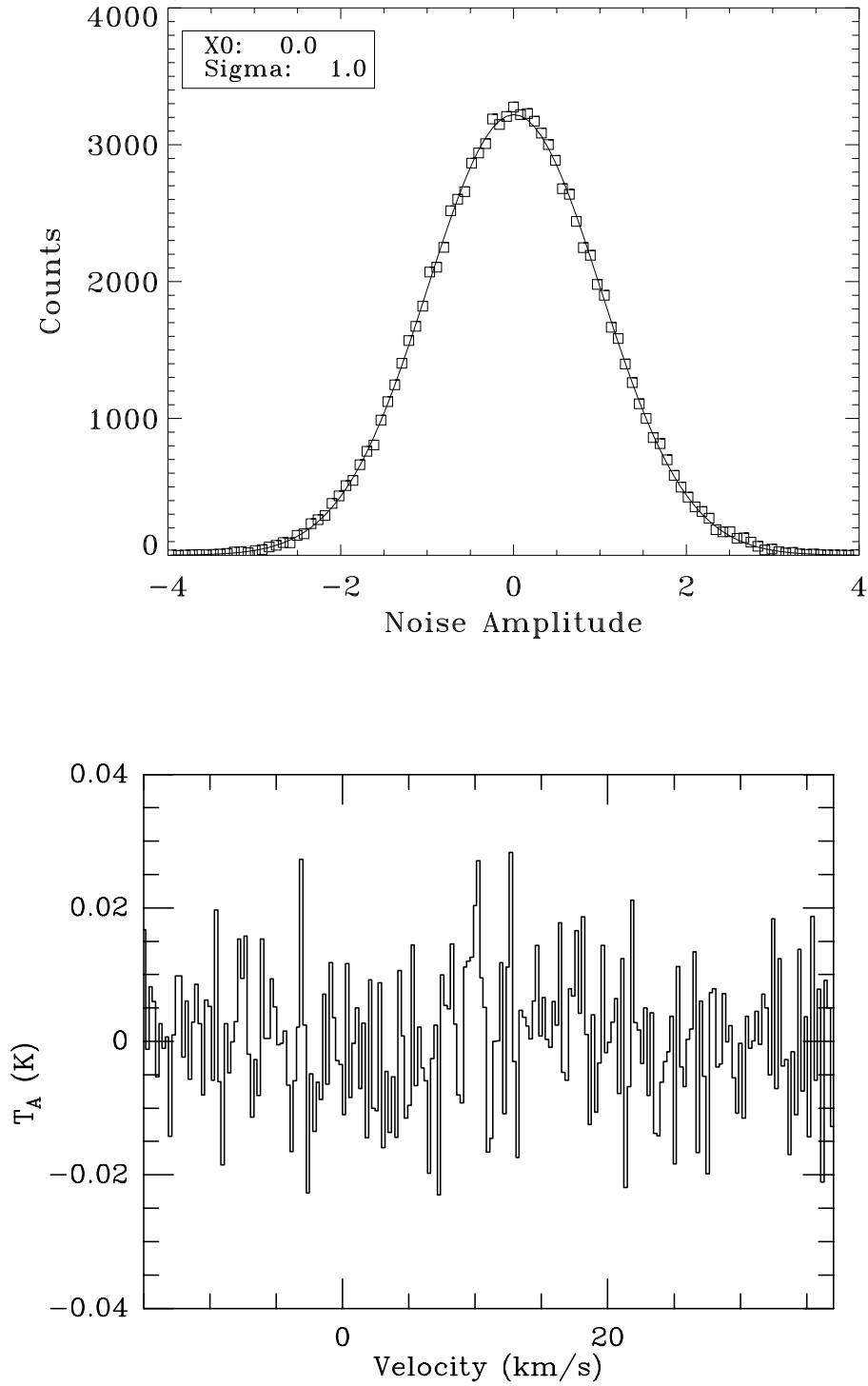


Fig. 4.— Distribution of a Gaussian random variable with zero mean ($X_0=0$) and unit variance ($\text{Sigma}=1$). In the upper panel, the squares indicates counts of generated values of the variable in each bin and the line indicates the fitted Gaussian. The lower panel is an example of such noise, with the RMS scaled to 0.01 K.

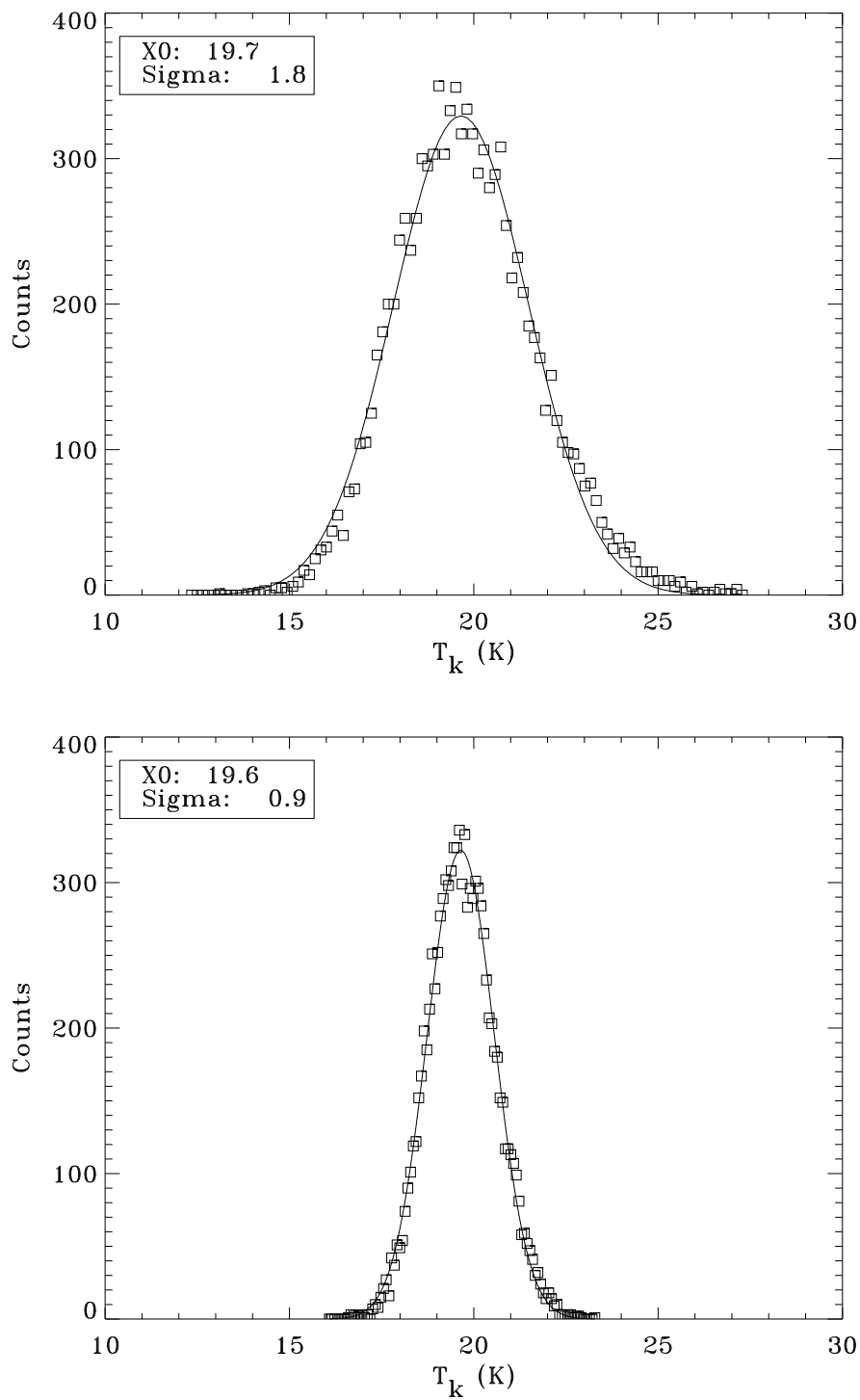


Fig. 5.— Distribution of kinetic temperatures obtained from artificially generated noisy NH_3 spectra whose RMS noise is 0.01 K. 10,000 pairs of noisy spectra were generated and used to calculate T_k . X0 and Sigma give the mean and the variance, respectively, of the samples of the derived kinetic temperatures. The kinetic temperature was 20 K in all cases. Upper panel: 5σ signal. Lower panel: 10σ signal.

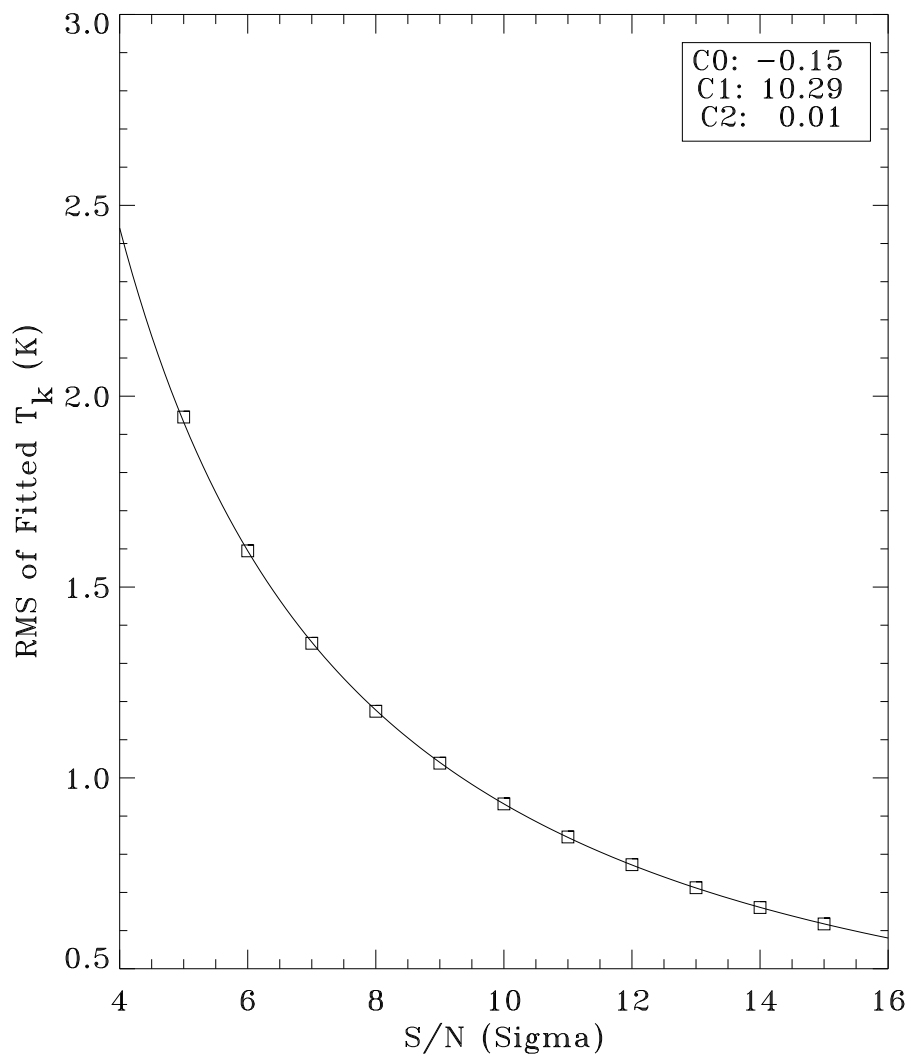


Fig. 6.— Uncertainty of the derived T_k vs. the S/N ratio of generated NH_3 spectra. Each point is based on 1000 pairs of (1,1) and (2,2) spectra with 0.01 K RMS noise and specified S/N ratio for the (2,2) line. The relative weakness of this line (found observationally) results in its S/N ratio being the determinant of T_k ; the S/N ratio of the (1,1) line is accordingly set to infinity. The solid line indicates the fitted function, $C_0 + C_1/(S/N) + C_2(S/N)$, with the three coefficients given in the box.

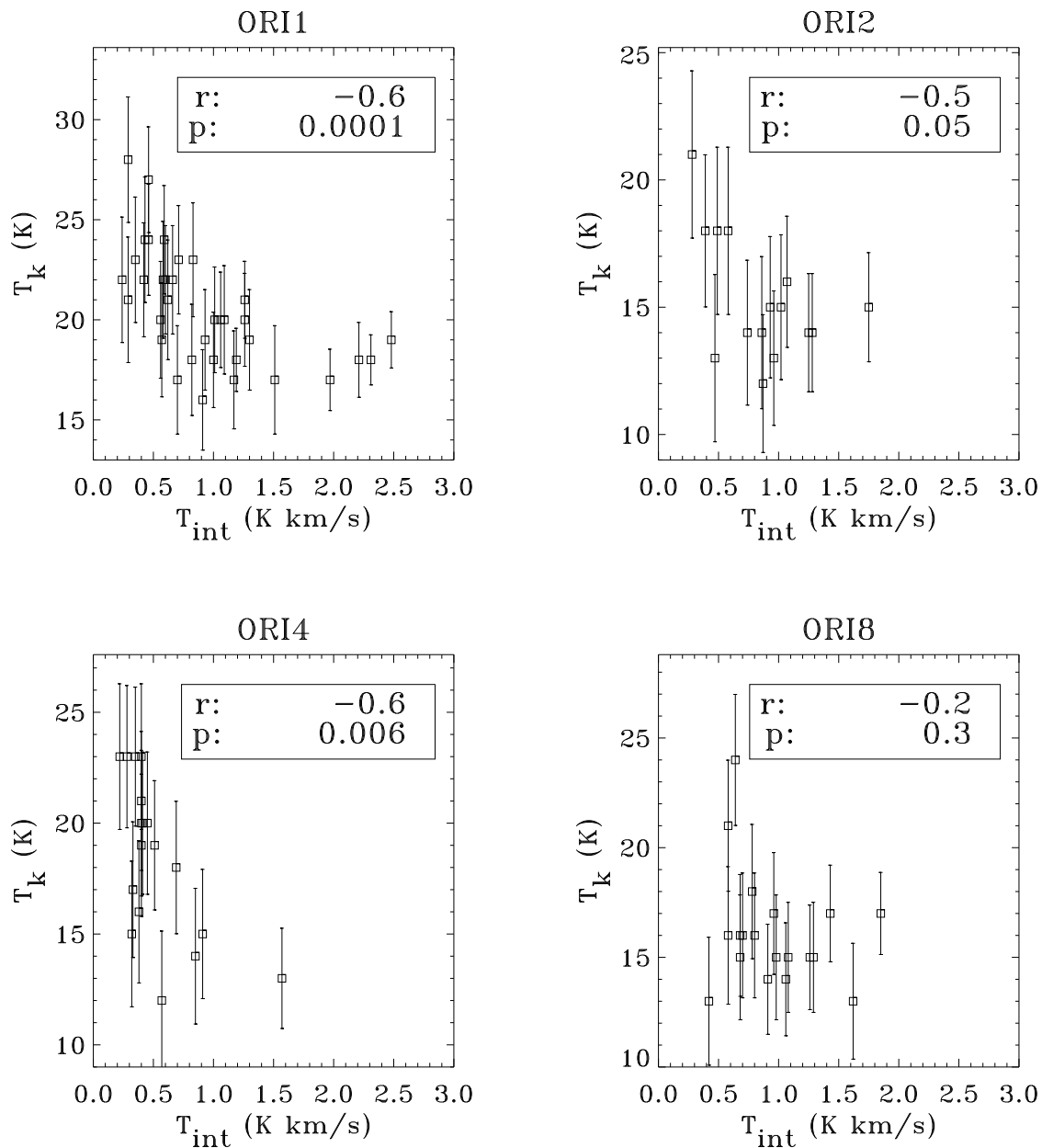


Fig. 7.— Correlations between integrated intensities of NH₃ (1,1) line and the derived T_k . The Pearson correlation coefficient r and the significance of the null hypothesis p (no correlation) are given in each small box. The error bars are at $\pm 1\sigma$ level, given by Eq. (7).

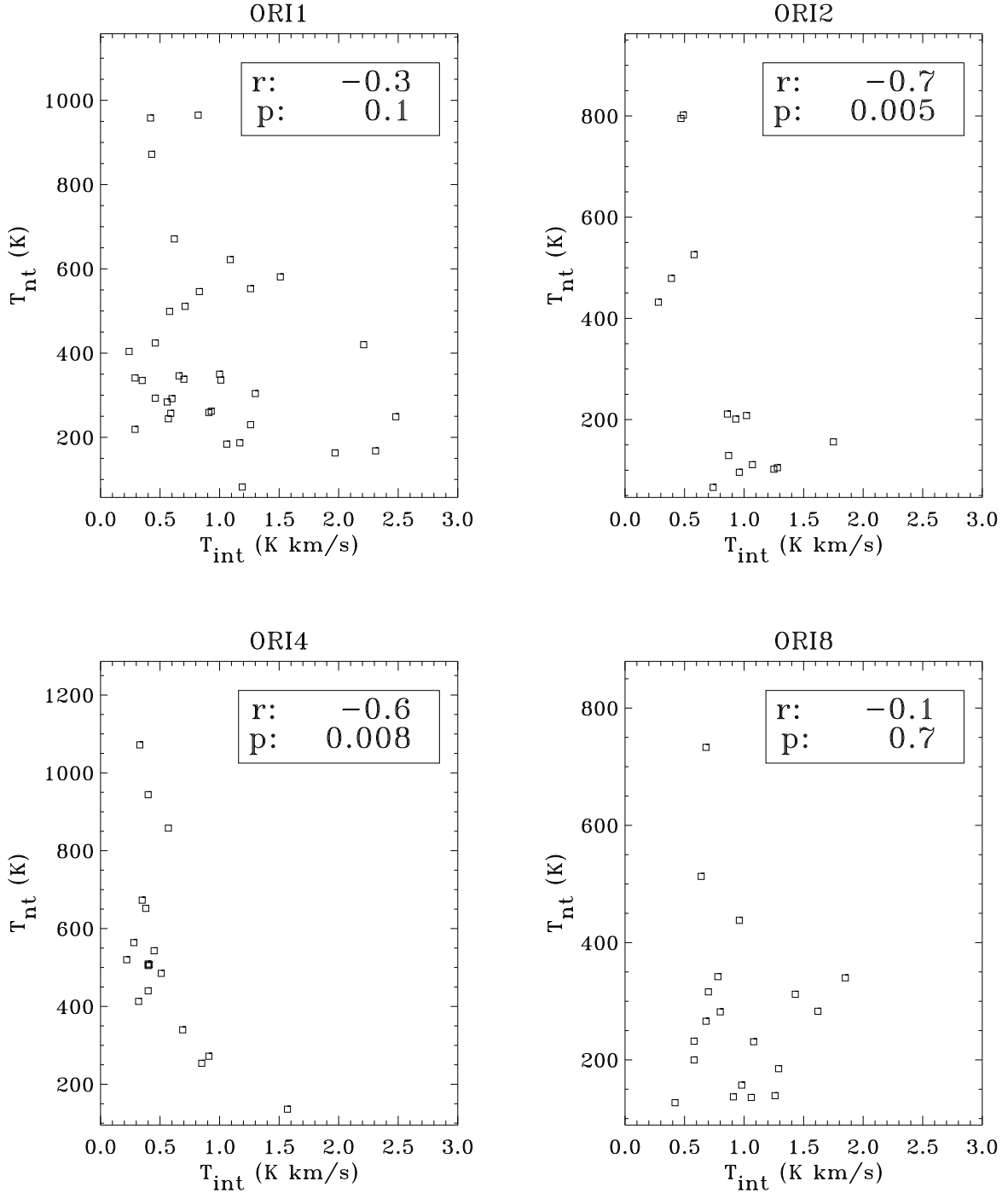


Fig. 8.— Correlations between integrated intensities of NH₃ (1,1) line and the turbulence measure T_{nt} . The Pearson correlation coefficient r and the significance of the null hypothesis p (no correlation) are given in each small box. The uncertainty in T_{nt} is about 5 K (see text).

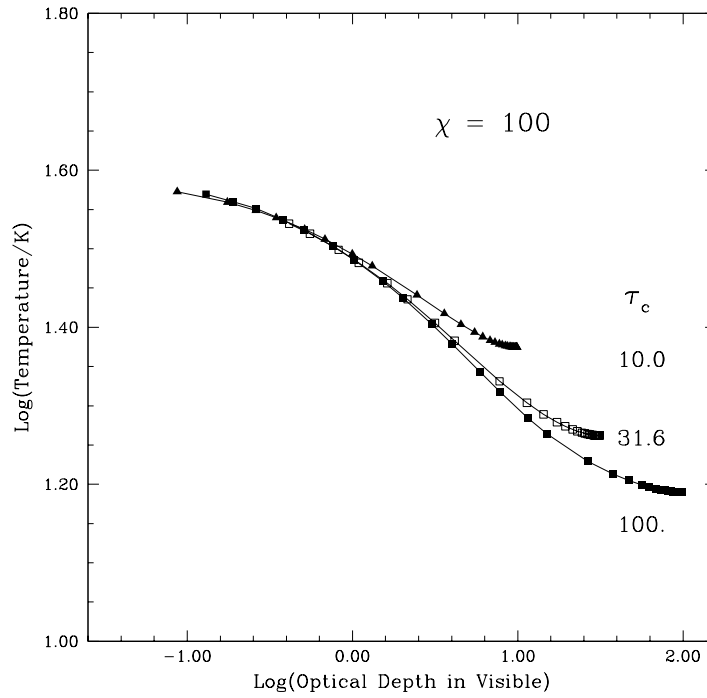
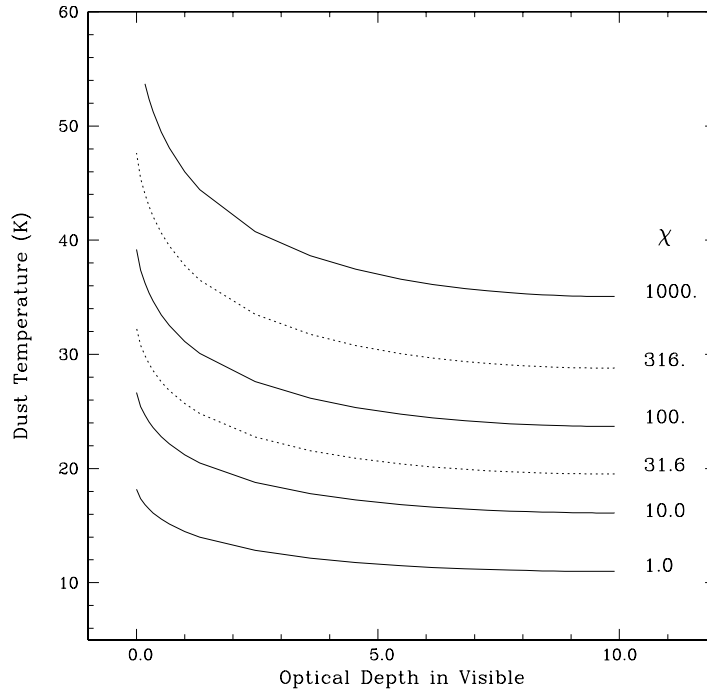


Fig. 9.— Upper panel:dust temperatures for clouds under different external radiation fields. χ is the factor by which the standard ISRF is multiplied. Lower panel: dust temperatures for clouds with total center-to-edge optical depths equal to 10, 31.6, and 100.

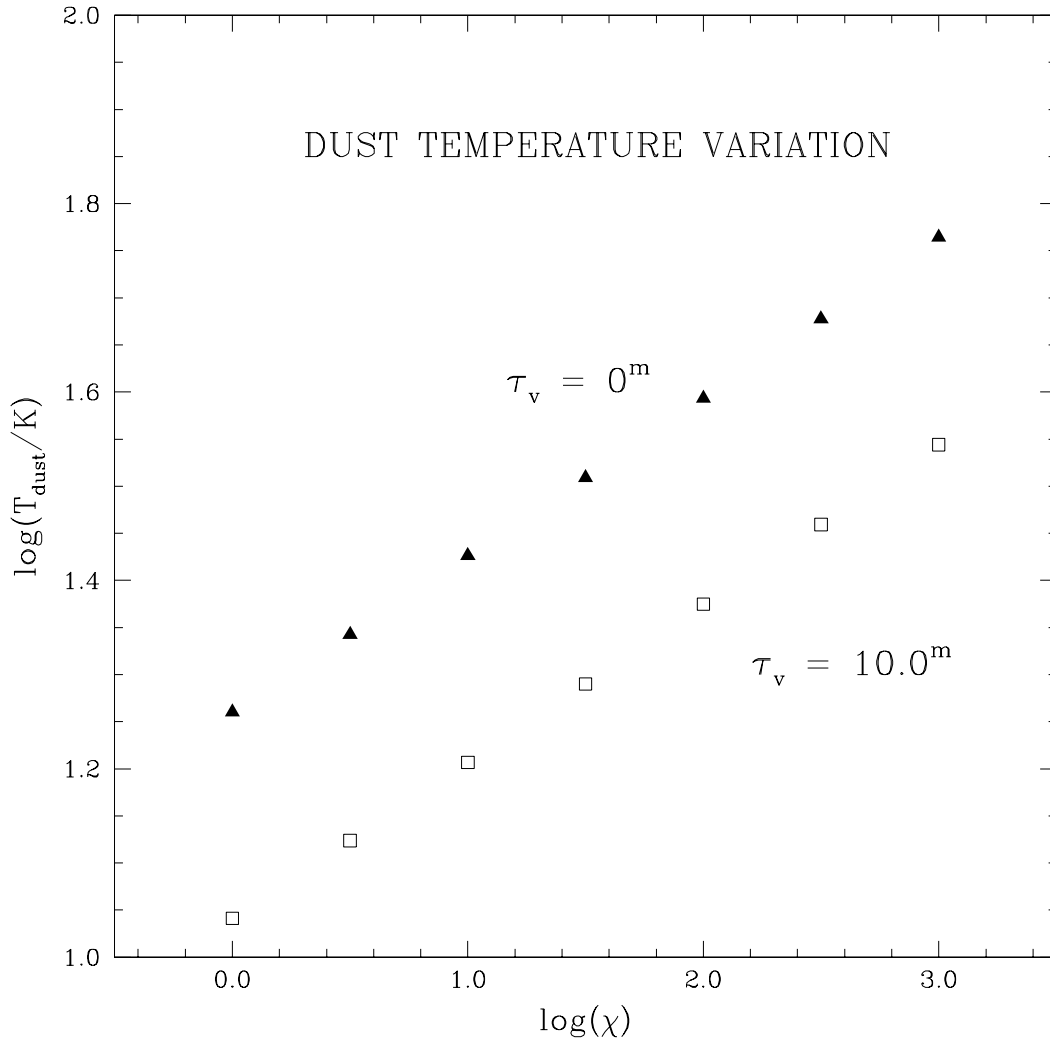


Fig. 10.— Dust temperatures at the cloud surface and at visual optical depth equal to 10. The power-law dependence of T_{dust} on χ , $T_{dust} \propto \chi^{1/6}$, is expected from the dust model used here (see discussion in the text).

Table 1. Core Parameters

Source	RA(1950) ^a h m s	DEC (1950) ^a d m s	V_{LSR} ^a km s ⁻¹	Δ RA ^b arcmin	Δ DEC ^b arcmin	N(C ¹⁸ O) 10 ¹⁵ cm ⁻²	N(NH ₃) ^c 10 ¹⁴ cm ⁻²	Δ V(NH ₃) ^c km s ⁻¹	T(NH ₃) ^d K	T(CO) ^e K	d_p ^f arcmin	Radius ^g arcmin	Mass M_{\odot}	n(H ₂) ^h 10 ⁴ cm ⁻³
ORI1	5 32 49.7	-5 02 23	10.6	0.0	0.0	13±2 ⁱ	3.3±1.3 ⁱ	0.85±0.07 ⁱ	19±1 ⁱ	33	23	1.4	260	20
ORI2	5 32 36.3	-5 59 43	8.4	2.0	1.5	6.5	2.7	0.68	15	20	34	2.6	360	4.5
ORI3	5 32 44.3	-6 01 43	8.2	NA	NA	NA	NA	NA	NA	25	36	NA	NA	NA
ORI4	5 33 37.9	-6 14 23	9.1	4.6	-0.7	5.3	4.5	0.63	15	23	51	2.3	250	4.8
ORI5	5 34 10.2	-6 15 03	8.2	-3.9	0.0	3.1	0.15	0.88	14	22	54
ORI6	5 34 02.0	-6 17 03	8.2	NA	NA	NA	NA	NA	NA	18	55	NA	NA	NA
ORI7	5 33 27.3	-6 28 23	8.8	2.8	2.2	4.5	0.30	0.69	14	28	64
ORI8	5 34 18.2	-6 26 23	8.2	1.5	-5.6	5.6	4.4	0.73	15	18	65	3.1	490	3.6
ORI9	5 33 38.0	-6 31 43	8.4	-1.5	-2.2	3.5	35	68
ORI10	5 33 54.1	-6 35 03	6.8	-0.7	2.2	4.1	12	72	1.9	106	3.5
ORI11	5 33 51.3	-6 41 43	7.0	0.7	-1.5	2.9	18	78	1.2	60	8.4
ORI12	5 33 48.8	-6 50 23	8.4	0.7	2.9	8.8	14	86
ORI13	5 36 03.3	-7 18 23	6.1	-1.5	0.0	2.3	15	123
ORI14	5 36 24.0	-7 26 23	5.4	2.2	2.9	3.3	10	132
ORI15	5 36 10.6	-7 28 23	5.6	0	-2.2	3.2	10	133

^aData are taken from the Orion CS survey (Tatematsu et al. 1993).

^bThe Offsets given in columns 2 and 3 are measured from the peak of the C¹⁸O integrated intensity to that of the CS. For ORI3 and ORI6, their C¹⁸O peaks (denoted as “NA”) are located at the same places as Ori2 and Ori4, respectively. This notation applies to other columns as well.

^cValues refer to the positions of strongest ammonia emission. For ORI5 and ORI7, the values are given for the (0,0) positions as given in columns 2 and 3 since NH₃ map is not available for these two sources. For all other source (“...”), the (2,2) line is not detected at a noise level of 0.03 K RMS.

^dKinetic temperature obtained from our ammonia observations. The values given refer to the positions of strongest ammonia emission, except for ORI3 and ORI6.

^eKinetic temperature based on CO 3-2 spectra (Wilson et al. 1999).

^fThe projected distance from the source to the Trapezium cluster.

^gThe square root of the product of semi-major and semi-minor axes. This size parameter is only given for cores whose C¹⁸O half intensity contours are enclosed by our 6′×6′ maps. The same is true for the last two columns of the table.

^hMean molecular hydrogen density obtained from C¹⁸O column density.

ⁱThe one σ statistical uncertainty resulting from a Gaussian fit to the spectra. The percentage is representative for this column. The uncertainty for the kinetic temperature is discussed in detail in section 4.2.